C. R. Mecanique 345 (2017) 11–20

Contents lists available at ScienceDirect

Comptes Rendus Mecanique

www.sciencedirect.com

Basic and applied researches in microgravity/Recherches fondamentales et appliquées en microgravité

Thermal convection in a cylindrical annulus under a combined effect of the radial and vertical gravity

Antoine Meyer [a], Marcel Jongmanns [b], Martin Meier [b], Christoph Egbers [b], Innocent Mutabazi [a,*]

[a] *Laboratoire "Ondes et milieux complexes", UMR 6294 CNRS – Université, Le Havre Normandie, 53, rue de Prony, BP 540, 76058 Le Havre cedex, France*

[b] *Department of Aerodynamics and Fluid Mechanics, Brandenburg University of Technology Cottbus-Senftenberg, Siemens-Halske-Ring 14, 03046 Cottbus, Germany*

ARTICLE INFO

Article history:
Received 8 March 2016
Accepted 7 April 2016
Available online 24 November 2016

Keywords:
Thermal convection
Cylindrical annulus
Dielectrophoretic buoyancy
Electric gravity
Thermal modes
Electric modes
Columnar modes
Microgravity
Parabolic flight experiment

ABSTRACT

The stability of the flow of a dielectric fluid confined in a cylindrical annulus submitted to a radial temperature gradient and a radial electric field is investigated theoretically and experimentally. The radial temperature gradient induces a vertical Archimedean buoyancy and a radial dielectrophoretic buoyancy. These two forces intervene simultaneously in the destabilization of the flow, leading to the occurrence of four types of modes depending on the relative intensity of these two buoyancies and on the fluid's properties: hydrodynamic and thermal modes that are axisymmetric and oscillatory, stationary columnar modes and electric modes which are stationary and non-axisymmetric modes. Experiments performed in a parabolic flight show the existence of non-axisymmetric modes that should be either columnar or helicoidal vortices.

1. Introduction

The alternating electric field with high enough frequency coupled with the temperature gradient gives rise to a dielectrophoretic force that can generate convective flows in a dielectric fluid [1,2]. In particular, it was that the dielectrophoretic force can be used to increase the heat transport in cylindrical systems [3,4]. The generation of convective motions by the dielectrophoretic force has been successfully tested in the GEOFLOW experiments that were performed in the Fluid Science Laboratory of the International Space Station where thermal convection patterns have been observed in a differentially rotating spherical shell submitted to a dielectrophoretic force [5,6]. Preliminary observations of the dielectrophoretic force effects in the cylindrical annulus were performed in parabolic flight experiments [7,8] where non-axisymmetric patterns were identified. The interest of the cylindrical annulus compared to spherical shells is the capacity of its implementations in the heat exchanger or in microfluidic systems. As the microgravity phase in parabolic flight experiments lasts only 22 s, it is necessary to perform an exhaustive investigation of the different effects of the control parameters of the flow systems in order to isolate the real contribution of the dielectrophoretic effect compared to the Archimedean buoyancy.

* Corresponding author.
E-mail address: innocent.mutabazi@univ-lehavre.fr (I. Mutabazi).

http://dx.doi.org/10.1016/j.crme.2016.10.003

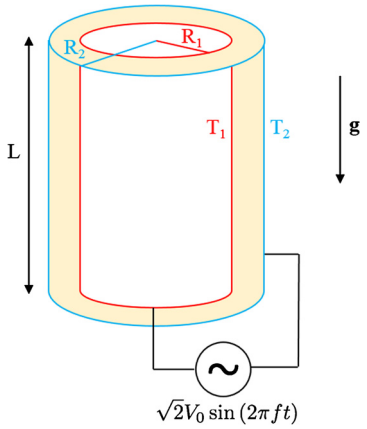

Fig. 1. Schematic sketch of the setup. The inner cylinder is heated and the voltage is applied to it. The outer cylinder is cooled and connected to the ground.

The present work presents the results of the linear stability analysis of the fluid (silicone oil) inside a cylindrical annulus with an alternating high-frequency electric field and a radial temperature gradient together with flow patterns observed during parabolic flight experiments. The paper is organized as follows: Section 2 describes the flow equations, and the results from linear stability analysis. Section 3 describes the experimental setup and the parabolic flight and presents preliminary experimental results realized in a recent parabolic flight campaign (October 2015). Discussion of the results and conclusion are addressed in sections 4 and 5.

2. Flow equations

We consider an incompressible dielectric fluid of density ρ, kinematic viscosity ν, thermal diffusivity κ and permittivity ε, confined between two concentric steady cylinders of length L and gap width d. The inner and outer cylinders of radii R_1 and $R_2 = R_1 + d$ are maintained at the temperatures T_1 and $T_2 < T_1$, respectively (Fig. 1). A high alternating electric potential is applied to the inner cylinder, while the outer one is grounded, resulting in an inhomogeneous inward directed electric field $\vec{E}$. The temperature difference between the cylinders induces the stratification in the density $\rho(T)$ and in the permittivity $\epsilon(T)$. The fluid density stratification in the Earth gravity field leads to the Archimedean buoyancy $\vec{F}_A = \delta\rho\vec{g}$, while the fluid permittivity stratification in the electric field leads to the dielectrophoretic force $\vec{F}_{\mathrm{d}} = \vec{E}^2\vec{\nabla}\epsilon$ [9]. The dielectrophoretic force dominates over the Coulomb force when the frequency of the electric field is very large compared to the inverse of the electric charge relaxation time $\tau_{\mathrm{e}} = \epsilon/\sigma_{\mathrm{e}}$, where σ_{e} is the electric conductivity [1]. In the Boussinesq approximation, all the fluid properties are assumed constant with respect to the temperature, except the density and permittivity in the Archimedean and dielectrophoretic forces, where they are assumed to vary linearly with the temperature, i.e. $\rho(T) = \rho_0[1 - \alpha(T - T_2)]$; $\varepsilon = \varepsilon_2[1 - e(T - T_2)]$, where ρ_0 and ε_2 are the density and permittivity at the reference temperature T_2.

The dielectrophoretic force can be written as follows [2]

$$\vec{F}_{\mathrm{DEP}} = \vec{\nabla}\left(\frac{\varepsilon_2 e\vec{E}^2(T - T_2)}{2}\right) - \rho\,\alpha\,(T - T_2)\,\vec{g}_{\mathrm{e}} \tag{1}$$

The conservative term can lumped into the pressure gradient and has effects only in the case of the interface dynamics. The non-conservative term represents the dielectrophoretic buoyancy induced by the effective electric gravity field $\vec{g}_{\mathrm{e}}$ given by:

$$\vec{g}_{\mathrm{e}} = \vec{\nabla}\left(\frac{e\,\varepsilon_2\,\vec{E}^2}{2\,\alpha\,\rho}\right) \tag{2}$$

The effective electric gravity represents the gradient of the electric energy stored in the capacitor. So a fluid particle is subject to a total gravity $\vec{G} = \vec{g} + \vec{g}_{\mathrm{e}}$.

Most of the time, the frequency of the electric potential is large enough compared to the inverses of the fluid characteristic times $\tau_\nu = d^2/\nu$ and $\tau_\kappa = d^2/\kappa$ so that only the time average dielectrophoretic buoyancy can affect the fluid motion. The electric contribution reduces to that of an effective static field.

In the following, we introduce the lengthscale d, the viscous diffusion timescale τ_ν, the temperature is scaled by $T_1 - T_2$ and the electric potential is scaled by the root mean square electric potential at the outer cylinder V_0. The flow equations for the velocity field $\vec{u}$, the temperature θ, the electric potential ϕ are derived from the conservation laws of the mass, the momentum, the energy, and the charge. Written in dimensionless form, they read:

$$\vec{\nabla}\cdot\vec{u} = 0 \tag{3}$$

$$\frac{\partial\vec{u}}{\partial t} + \vec{u}\cdot\vec{\nabla}\vec{u} = -\vec{\nabla}\pi + \Delta\vec{u} + Gr\theta\vec{e}_z - \frac{V_E^2}{Pr}\gamma_e\theta\vec{g}_e \tag{4}$$

$$\frac{\partial\theta}{\partial t} + \vec{u}\cdot\vec{\nabla}\theta = \frac{1}{Pr}\Delta\theta \tag{5}$$

$$\vec{\nabla}\cdot\left[(1-\gamma_e\theta)\,\vec{\nabla}\phi\right] = 0, \quad \vec{E} = -\vec{\nabla}\phi \tag{6}$$

where $Pr = \nu/\kappa$ is the Prandtl number, $Gr = \alpha\Delta T G d^3/(\nu^2)$ is the Grashof number ($G = g$ in the gravity phase and $G = 1.8\,g$ in the hypergravity phase), $\Delta T = T_1 - T_2$, $\gamma_a = \alpha\Delta T$ is the thermal expansion parameter, $\gamma_e = \epsilon\Delta T$ is the thermoelectric parameter, $V_E = V_0/\sqrt{\rho\nu\kappa/\varepsilon_2}$ is the dimensionless electric potential difference. The generalized pressure π is given by:

$$\pi = \frac{P}{\rho} - \frac{e\,\theta\,\varepsilon_2\,E^2}{2\,\rho} - \frac{1}{2}\left(\frac{\partial\varepsilon}{\partial\rho}\right)_\theta E^2 \tag{7}$$

The equation (6) stems from the Gauss law of the electric flux conservation in the dielectric fluid when the electric permittivity varies with the temperature. The boundary conditions on the two cylinders read:

$$\begin{cases} \vec{u} = \vec{0}, & \theta = 1, & \phi = 1 & \text{at } r = \eta/(1-\eta) \\ \vec{u} = \vec{0}, & \theta = 0, & \phi = 0 & \text{at } r = 1/(1-\eta) \\ \vec{u} = \vec{0}, & \partial\theta/\partial z = 0 & \partial\phi/\partial z = 0 & \text{at } z = 0 \text{ and } \Gamma \end{cases} \tag{8}$$

where $\eta = R_1/R_2$ is the radius ratio and $\Gamma = L/d$ is the aspect ratio.

The parabolic flight experiment was performed with an applied electric field during the whole parabolic flight; this means that the electric gravity was acting during the whole experiment. The gravity and hypergravity phases of the parabolic flight can be taken into account by a crude approximation that neglects the time dependence of the vertical gravity G.

2.1. Base state

In the case of infinite length cylindrical annulus ($\Gamma \to \infty$), the system of equations governing the flow admits a stationary axisymmetric and axially invariant base state. The temperature and the axial velocity profile are given by [10]:

$$\Theta(r) = \frac{\ln[(1-\eta)r]}{\ln(\eta)} \tag{9}$$

$$W = \frac{Gr}{Re}\left(C\left[(1-\eta)^2 r^2 - 1 + (1-\eta)^2\,\Theta\right] - \frac{r^2\,(1-\eta)^2 - \eta^2}{4\,(1-\eta)^2}\Theta\right) \tag{10}$$

where the coefficient C is

$$C = \frac{\left(1-\eta^2\right)\left(1-3\eta^2\right) - 4\eta^4\log\eta}{16\,(1-\eta)^2\left[\left(1-\eta^2\right)^2 + \left(1-\eta^4\right)\log\eta\right]} \tag{11}$$

The radial temperature gradient induces an axial flow with velocity profile $W(r)$ where the fluid flows upward near the hot surface and downward near the cold surface. The electric potential is obtained from the Gauss law (6) and reads

$$\Phi = \frac{\ln(1-\gamma_e\Theta)}{\ln(1-\gamma_e)} \tag{12}$$

The electric gravity of the base state is always centripetal when the temperature gradient is outward, while it can change the sign in the case of inward heating for large values of the radius ratio [2].

$$\vec{g}_{e,b} = -g_0 F(\gamma_e,\eta,r)\vec{e}_r, \quad g_0 = \frac{e\,\epsilon_2\,V_0^2}{\rho_0\,\alpha\,(\ln\eta)^2\,r^3}$$
$$F = \left[\frac{\gamma_e}{\ln(1-\gamma_e)}\right]^2\left[1-\gamma_e\left(\frac{\Theta(r)}{\Delta T} + \frac{1}{\ln\eta}\right)\right]\left[1-\gamma_e\frac{\Theta(r)}{\Delta T}\right]^{-3} \tag{13}$$

The generalized gravity is inclined in the meridional plane (r, z).

2.2. Linear stability analysis

The stability of the base state is performed by adding an infinitesimal perturbation $(u', v', w', \pi', \theta', \phi')$ into the flow equations (3), (4), (5), (6) and neglecting second and higher order terms in perturbations. The invariance in the axial and azimuthal directions allow for the development of the perturbations into normal modes of the form $(\hat{u}, \hat{v}, \hat{w}, \hat{\pi}, \hat{\theta}, \hat{\phi})\, e^{st+in\varphi+ikz}$, where s is the complex growth rate, k is the axial wavenumber and n is the azimuthal mode number. The hatted quantities are complex amplitudes of perturbations that only depend on the radial coordinate. The resulting governing equations are given by:

$$0 = \left(D + \frac{1}{r}\right)\hat{u} + \frac{in}{r}\hat{v} + ik\hat{w} \tag{14}$$

$$s\hat{u} = \left(\Delta - \frac{1}{r^2} - ikW\right)\hat{u} - \frac{2in}{r^2}\hat{v} - D\hat{\pi} - \frac{\gamma_e V_E^2}{Pr}\left(-\hat{\theta}G_e + \hat{g}_{e,r}\Theta\right) \tag{15}$$

$$s\hat{v} = \frac{2in}{r^2}\hat{u} + \left(\Delta - \frac{1}{r^2} - ikW\right)\hat{v} - \frac{in}{r}\hat{\pi} - \frac{\gamma_e V_E^2}{Pr}\hat{g}_{e,\varphi}\Theta \tag{16}$$

$$s\hat{w} = (DW)\,\hat{u} + (\Delta - ikW)\,\hat{w} - ik\hat{\pi} + Gr\hat{\theta} - \frac{\gamma_e V_E^2}{Pr}\hat{g}_{e,z}\Theta \tag{17}$$

$$s\hat{\theta} = -(D\Theta)\,\hat{u} + \left(\frac{1}{Pr}\Delta - ikW\right)\hat{\theta} \tag{18}$$

$$0 = -\gamma_e\left[D\Phi D + \frac{1}{r}D\Phi + \left(D^2\Phi\right)\right]\hat{\theta} + [(1 - \gamma_e\Theta)\,\Delta - \gamma_e D\Theta D]\,\hat{\phi} \tag{19}$$

where $D = d/dr$, and $\Delta = d^2/dr^2 + d/rdr - (n^2/r^2 + k^2)$ is the Laplacian operator. The complex amplitude of perturbation electric gravity $(\hat{g}_{e,r}, \hat{g}_{e,\varphi}, \hat{g}_{e,z})$ has been introduced:

$$\hat{g}_{e,r} = \left(D\Phi D^2 + D^2\Phi D\right)\hat{\phi}\,, \quad \hat{g}_{e,\varphi} = \frac{in}{r}D\Phi D\hat{\phi}\,, \quad \hat{g}_{e,z} = ikD\Phi D\hat{\phi} \tag{20}$$

The boundary conditions for the amplitude of perturbations read:

$$\hat{u} = \hat{v} = \hat{w} = D\hat{u} = \hat{\theta} = \hat{\phi} = 0 \quad \text{at } r = \frac{\eta}{1-\eta}\,;\frac{1}{1-\eta} \tag{21}$$

Equations (14)–(19) and (21) are invariant by the operation $(n, \hat{v}) \to (-n, -\hat{v})$. It means that once the eigenvalue s and the corresponding eigenfunctions $(\hat{u}, \hat{v}, \hat{w}, \hat{\pi}, \hat{\theta}, \hat{\phi})$ are known for a given mode (n, k), the mode $(-n, k)$ will give the same eigenvalue s with the eigenfunctions $(\hat{u}, -\hat{v}, \hat{w}, \hat{\pi}, \hat{\theta}, \hat{\phi})$. The stability conditions for both modes are identical. The eigenvalue problem is discretized by a Chebyshev spectral collocation method and is solved by a QZ decomposition. To ensure the convergence of the computation, the highest order of the Chebyshev polynomials is set at 30.

The eigenvalue $s = \sigma + i\omega$ is computed for a given set of parameters $(Pr, \eta, \gamma_e, Gr, V_E, n, k)$. When the maximum value of the growth rate real part σ is equal to zero, we have got the marginal state. Marginal curves can be plotted in the plan (k, V_E) or (k, Gr) for different azimuthal mode number n. The global minimum of these curves corresponds to the critical state denoted by $(Gr_c, V_{Ec}, n_c, k_c, \omega_c)$, where ω_c is the critical frequency of vortex propagation. The total wavenumber of the critical mode q_c gives the wavenumber measured along the transversal direction to the rolls at the median surface between the two electrodes, and is defined as:

$$q_c = \sqrt{k^2 + k_n^2} \quad \text{where} \quad k_n = \frac{2(1-\eta)}{1+\eta}n_c \tag{22}$$

2.3. Critical parameters

The linear stability analysis was performed for the silicone oil AK5 with $Pr = 64.6$ and $\gamma_a/\gamma_e = 1.01$, in an infinite-length cylindrical annulus with radius ratio $\eta = 0.5$ in the natural gravity. For this flow configuration, $Gr/\gamma_a = 228$. In the absence of electric potential, we recover the critical modes in the form of oscillatory axisymmetric vortices of the thermal instability [10]. When the electric potential is applied to the flow system, the threshold remains constant until the potential reaches $V_E = 100$ and then starts to decrease (Fig. 2a). The critical axial wavenumber and the critical frequency (Fig. 2b, d, e) are nearly independent of V_E. This means that for this regime, the thermoelectric buoyancy plays a passive role. For $V_E = V_E^* = 425$, the critical mode changes from an oscillatory axisymmetric mode to stationary columnar vortices with axis parallel to the cylindrical axis, i.e. $k_c = 0, n_c \neq 0, \omega_c = 0$. The threshold of this mode strongly decreases with the electric potential, but the azimuthal wavenumber is constant with respect to V_E. For $V_E = V_E^{**} = 3800$, the columnar vortex mode disappears and the critical mode is formed of inclined stationary vortices corresponding to the electric mode obtained in zero-gravity conditions [2]. The axial wavenumber increases with V_E before it saturates, while the azimuthal wavenumber

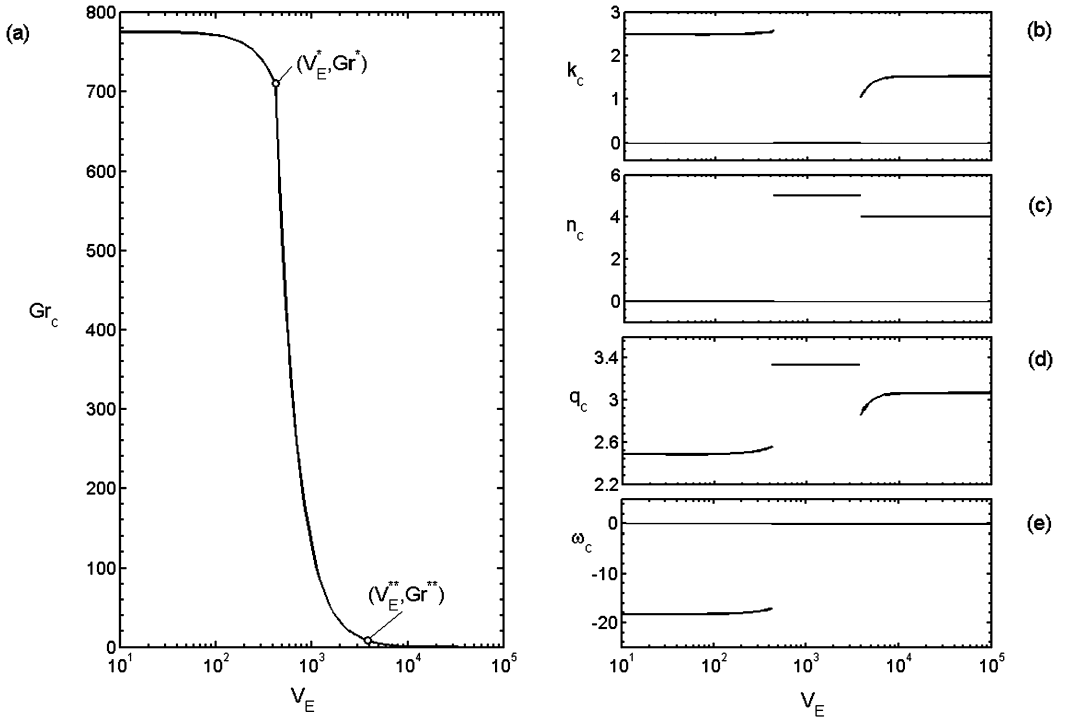

Fig. 2. Behavior of (a) the critical Grashof number, (b) the critical axial wavenumber, (c) the azimuthal wavenumber, (d) the critical total wavenumber, and (e) the critical frequency with the dimensionless electric potential.

is constant. For $V_E > V_E^{**}$, the critical Grashof number decreases and tends to zero for large values, i.e. $V_E >> V_E^{**}$. In this flow, there exist two codimension-2 points: the point V_E^*, Gr^* separating the thermal mode and the columnar vortex mode and the point V_E^{**}, Gr^{**} separating the columnar vortex mode and the electric mode. The thermal modes are due to the Archimedean buoyancy, while the electric modes are generated by the dielectrophoretic buoyancy. The columnar modes are the result of the interplay between the Archimedean and the dielectrophoretic buoyancies.

3. Experiment

3.1. Parabolic flight campaign

The parabolic flight is a cheap way to create a microgravity condition on Earth and it gives us the opportunity to investigate the fluid behavior in three different gravity conditions. Initially the plane flies at a constant altitude and velocity, it experiences a vertical gravity intensity of $1\,g$. The plane is then accelerated and pulled up during 20 s and the vertical gravity intensity increases up to $1.8\,g$. At the end of this phase, the planes' nose is about 47° to the horizon. Then the engines are throttled and the plane stops to accelerate. The plane follows a parabolic trajectory to hold the microgravity phase, which lasts about 22 s. After the microgravity phase, a second hypergravity phase up to $1.8\,g$ is experienced and the plane goes back to a steady, horizontal flight. The quality of the microgravity phase is about $10^{-2}g$, which is sufficiently small to assume a purely radial gravity in the experiment. However, the duration of this phase remains too short for getting a steady convective state.

3.2. Experimental setup

The experiment cell consists of two concentric cylinders: the radius of the inner one is $R_1 = 5.1$ mm and that of the outer one is $R_2 = 10.2$ mm, the gap width is $d = 5.1$ mm and its length is $L = 100$ mm (Fig. 1). Thus, the radius ratio is $\eta = 0.5$, and the aspect ratio is $\Gamma = 19.6$. The properties of the working fluid (silicone oil Wacker AK5) inside the cylindrical annulus are given in Table 1. So the viscous diffusion is $\tau_\nu = 5.2$ s, and the thermal diffusion time is $\tau_\kappa = Pr\tau_\nu = 336$ s.

The inner cylinder is made of aluminum oxide (Al_2O_3) and coated with titanium nitride (TiN) to create a conductive layer. The applied ac-peak voltage is V_{peak} ($V_0 = \sqrt{2}\,V_{\text{peak}}/2$) with a frequency of 200 Hz corresponding to a period of $T = 5 \times 10^{-3}$ s, which is very small compared to the viscous diffusion time. Table 2 gives the correspondence between the applied electric tension V_{peak} and the dimensionless electric potential V_E. A heating cartridge with a temperature sensor is located inside the inner cylinder. The outer cylinder, made of aluminum (AlMgSi0.5) is connected to the ground potential and is cooled by a cooling fluid loop, which also uses AK5. The top and bottom lids are made of polymethylmethacrylate

Table 1
Properties of silicone oil AK5: $\varepsilon_r = \varepsilon_2/\varepsilon_0$ is the relative electric permittivity, ε_0 is the permittivity of the vacuum. Property data are given by the manufacturer and have uncertainties, e.g., 10% for the kinematic viscosity.

ν (10^{-6} m^2/s)	ρ (kg/m^3)	α (10^{-3} K^{-1})	ϵ_r	e (10^{-3} K^{-1})	Pr	α/e
5.0	920	1.08	2.70	1.07	64.6	1.01

Table 2
The electrical dimensionless potential corresponding to different voltages V_{peak} imposed at the inner cylinder.

	4 kV	5 kV	6 kV	7 kV	8 kV	9 kV
V_E	732	916	1099	1283	1466	1649

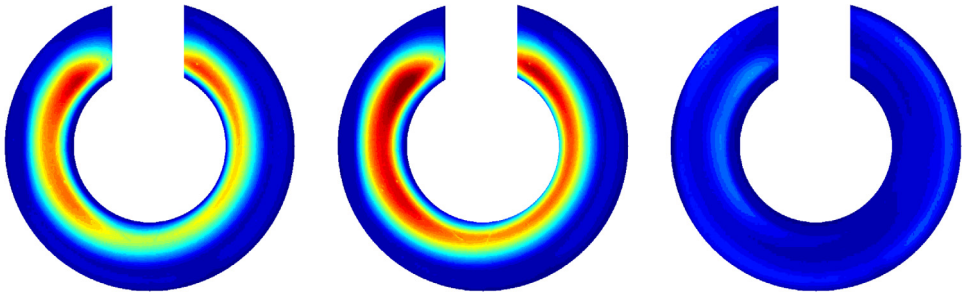

Fig. 3. The shadow image of the base flow in the vertical cell without applied electric field and with $\Delta T \approx 10$ K for (a) $G = 1\,g$, (b) $G = 1.8\,g$ and (c) $G = 0$. These images have the same color scale.

(PMMA) to ensure thermal and electrical insulation. Since the inner cylinder is thin (1.85 mm) and has a good thermal conductivity, we considered that the temperature measured by the heating cartridge corresponds to the temperature of the inner cylinder. With this heating and cooling system it is possible to generate a temperature difference between the inner and outer cylinder of up to 12 K.

To visualize the flow pattern, a shadowgraph method was used. The cell is illuminated from the bottom by a LED with telecentric lighting. The light goes through the liquid in the cell and is refracted because of density gradients inside the fluid. When the temperature changes, the density and the refractive index of the fluid change, and the flow also changes. The image of the flow changes is captured with a camera, which is focused on the top of the cell. To enhance the contrast, a false color representation is used. Since the refractions are integrated over the height of the cell and the cell has a large height, it is impossible to make calculations with the obtained data. The shadowgraph method gives only the qualitative behavior of the convective flow.

In the base state of the flow when the heating system is active, but there is no additional force field other than the Earth gravitation; it can be expected that there is an upward flow at the heated inner cylinder and a downward flow at the cooled outer cylinder. Such a structure can be seen with this visualization method (Fig. 3a, b). The comparison of the flows between the gravity ($1\,g$) and the hypergravity ($1.8\,g$) phases with active heating, in the absence of the electric field, shows nearly no difference between the states (Fig. 3), whereas in the (μg-) phase (Fig. 3c), no flows can be observed. This observation corresponds to the almost homogeneous vertical temperature distribution during the last seconds of the μg-phase shown in Fig. 4.

3.3. Flow patterns

The temperature difference between both cylinders for all experimental runs was fixed at $\sim$10 K and the voltage was varied, but active the whole time. The temperature is measured on six positions at the inner surface of the outer cylinder (Fig. 4). The temperature sensor at the top of the cell (TS5) gives a temperature of about 22 °C, while the sensor at the bottom (TS0) of the cell gives the lowest value. The microgravity phase disrupts this natural thermal convection.

The application of the electric field modifies the structures in the flow (Fig. 5). While in $1g$-condition, vortices start to form at $V_0 \simeq 4.24$ kV, they are observed at $V_0 = 3.54$ kV under microgravity conditions. Due to the limited duration of the microgravity phase ($\Delta t_{\mu g} \sim 22$ s), the flow does not have enough time to fully develop. Increasing the strength of the electric field increases the growth rate of vortices, i.e. it decreases the time needed for them to develop and their intensity. (Fig. 6). The comparison of the results from $1\,g$ and $\mu\,g$ conditions at the same potential $V_0 = 6.36$ kV shows that there is still a big influence of the Earth gravity (Fig. 6).

Fig. 6 shows images of the perturbed state at different steps of a parabola where $V_0 = 6.36$ kV. The patterns observed at the end of the normal gravity phase (Fig. 6a) and at the end of the hypergravity phase (Fig. 6b) are similar. The shape of

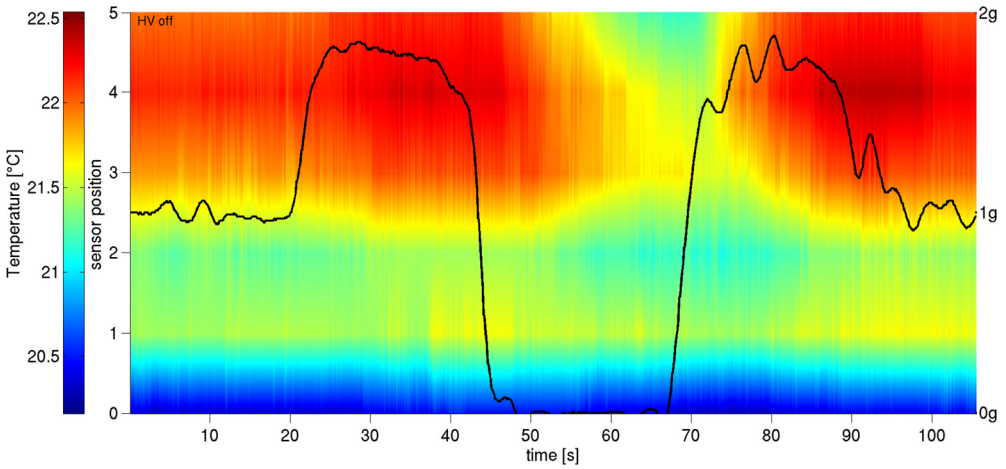

Fig. 4. Vertical temperature distribution at the outer cylinder over one parabola without electric field. The solid line represents the gravity variation in time along the parabolic flight for 110 s.

Table 3
Critical dimensionless electric potential for the different states of gravity.

		μg	$1\,g$
V_{Ec}	Theory	473	479
	Experiment	$732 < V_{Ec} < 916$	$916 < V_{Ec} < 1099$

the unstable mode is the same for both cases. The pattern observed at the first moment of the microgravity phase (Fig. 6c) is a consequence of the characteristic flow of the previous hypergravity phase. This initial condition progressively disappears during the first 10 s of the microgravity phase. After about 10 s of this phase, the perturbed flow related to the radial artificial gravity starts to grow.

4. Discussion

The linear stability analysis of the conduction regime, valid for an infinite-length cylinder, shows that, in a fluid with $Pr = 64.6$ inside a cylindrical annulus, the threshold is $Gr_c = 775$ and the critical thermal mode appears in form of oscillatory axisymmetric vortices. The temperature difference $\Delta T = 10$ K with the chosen working fluid corresponds to $Gr = 562 < Gr_c$ for $G = g$ and to $Gr = 1011.6 > Gr_c$ for $G = 1.8\,g$. Thus, in the g-phase, no instability would be expected, while it is expected for $G = 1.8\,g$. In the microgravity phase, $G = 0.01\,g$ corresponds to $Gr = 5.6$ for our experimental setup. So when there is no applied electric potential ($g_e = 0$), the instability of the flow is expected only in the hypergravity phase. The visualization by the shadowgraph technique does not allow for observation of axisymmetric patterns. In our experiment, the electric potential was always applied so that the effective gravity acting on the fluid had an electric component. If any structure is observed by shadowgraph, it should be either helicoidal or columnar vortices. Table 3 compares the critical values of the dimensionless electric potential for different states of the gravity from the linear stability analysis and the experiment.

However, the aspect ratio used in the experiment is relatively small to neglect the boundary layers from the endplates and to ensure the conduction regime of the base state which was assumed in the linear stability analysis. In fact, according de Vahl Davis and Thomas [11], the conduction regime is realized if $Gr < 400\Gamma/Pr$ and the transition regime occurs when $400\Gamma/Pr < Gr < 3000\Gamma/Pr$; for $Gr > 3000\Gamma/Pr$, the flow is in the boundary layer regime. For our experimental conditions, the conduction regime exists for $Gr < 121.4$, the transition regime exists for $121.4 < Gr < 910.2$, and the boundary regime for $Gr > 910.2$. Therefore, the comparison with the linear stability results is realistic only in the microgravity phase. Moreover, the time variation of the total gravity G was neglected. These comments appeal for direct numerical simulation of the flow equations to take into consideration the realistic base state and the time dependence of the total gravity.

The experiments were performed using the shadowgraph technique to visualize the flow patterns integrated over the whole height of the fluid. This technique does not allow us to obtain quantitative data. We have tested the back-oriented-schlieren (BOS) technique, but it was not successful along the parabolic flight experiment. For the next parabolic flight campaign, a new set of experimental cells is under preparation with small height to face some of the problems of BOS.

5. Conclusion

The present work addresses the stability of a dielectric liquid with a high Prandtl number under a combined action of the Earth gravity and of an electric gravity. A theoretical analysis show that the resulting modes are either columnar or

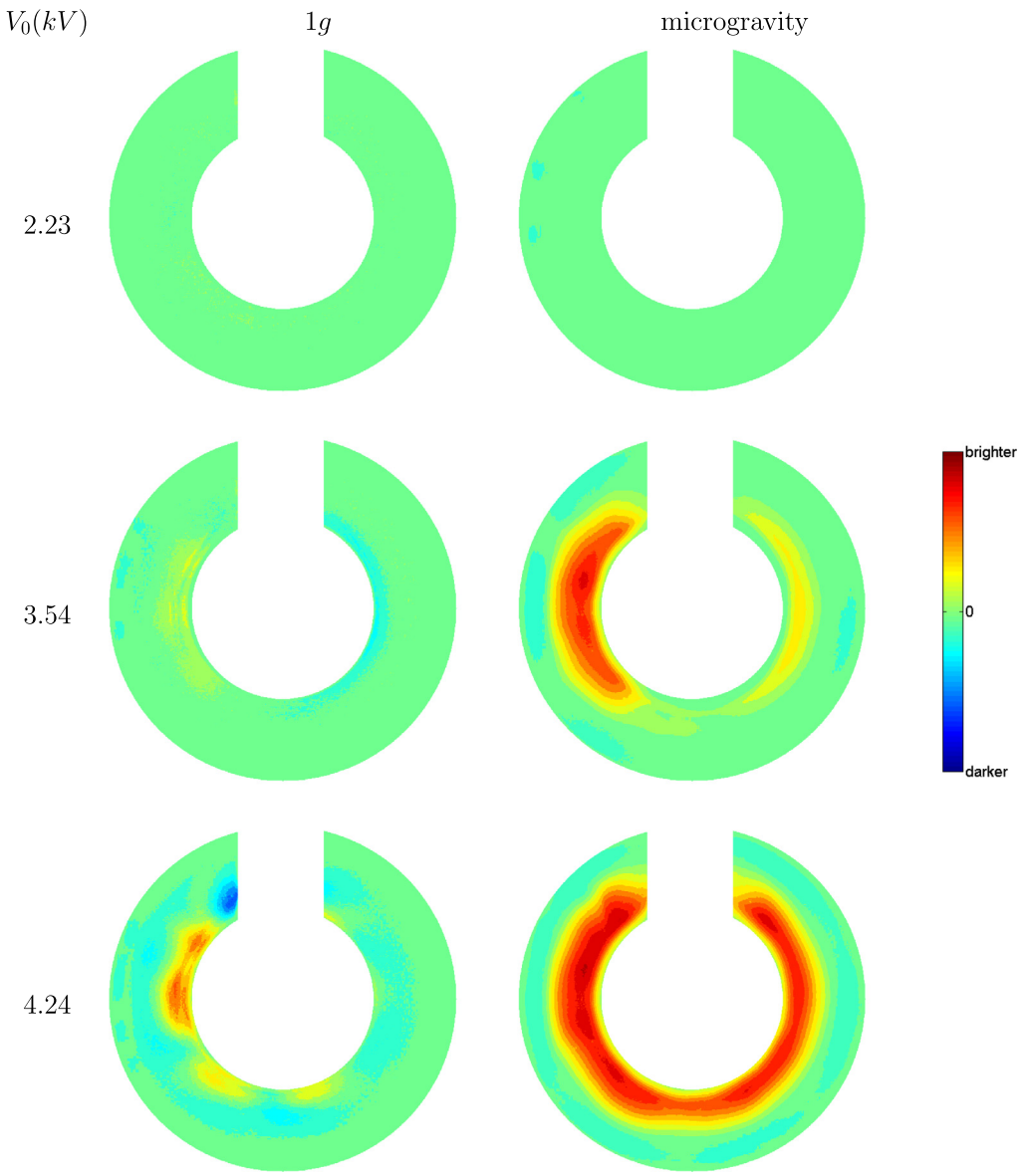

Fig. 5. Patterns of the light intensity distribution diminished by the one of the basic state of the corresponding gravity phase (Fig. 3) for different gravity phases and different applied electric tension with $\Delta T \approx 10$ K. A disruption of the base flow occurs between 3.54 kV and 4.24 kV in 1 g, while it is earlier in microgravity.

electric modes. Experiments performed in a parabolic flight confirm the existence of non-axisymmetric modes. A further investigation is needed for a better description of this complex problem with realistic conditions, in particular the time dependence of gravity during the different phases of the parabolic flight.

Acknowledgements

The present work was realized with the support from the “Centre national d’études spatiales” (CNES) (grant No. 160483/25). The authors are grateful to NOVESPACE for providing technical help during the parabolic flight campaign. Fruitful discussions with O. Crumeyrolle and H. Yoshikawa are recognized. I.M. thanks the support from the CPER Haute-Normandie (THETE) and the Agence Nationale de la Recherche (ANR), through program “Investissements d’avenir” (ANR-10 LABX-09-01), LABEX EMC^3. A.M. benefits from the doctoral scholarship from the Normandie Region Council. M.J., C.E. and M.M. acknowledge the partial support by the German Aerospace Center (DLR) within the “GeoFlow” project (grant No. 50 WM 0822) and the project “Convection in concentric gaps (KIKS)” (grant No. 50WM1644). This work is a part of the CNRS LIA 1092 ISTROF.

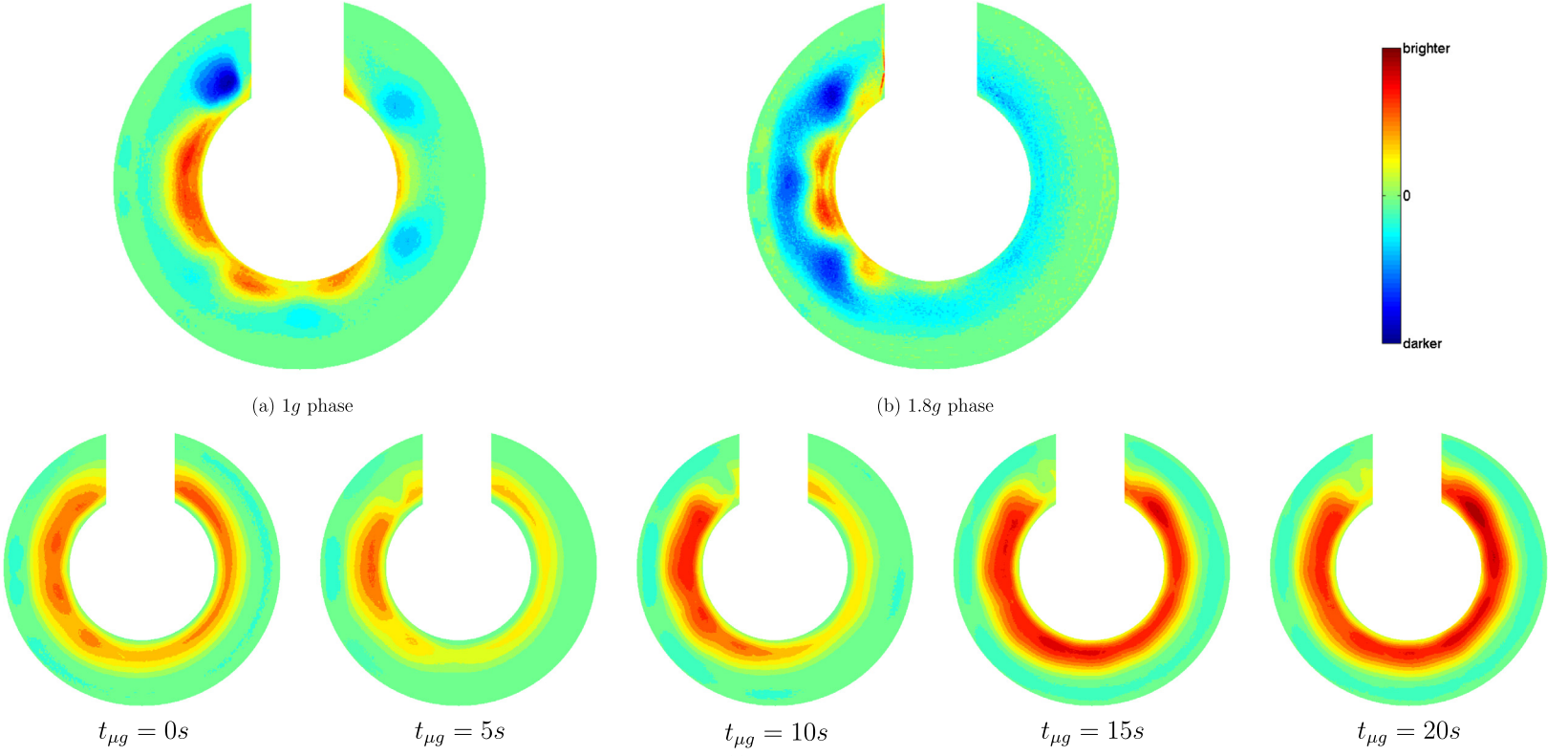

Fig. 6. Patterns of the light intensity distribution diminished by the one of the basic state of the corresponding gravity phase (Fig. 3). All images are captured at $V_0 = 6.36$ kV and $\Delta T \approx 10$ K. The images (a) and (b) are taken at the end of the $1\,g$ and $1.8\,g$ phases, respectively. The images (c) show a time sequence under microgravity conditions where $t_{\mu g} = 0$ stands for the first allowable moment of the microgravity phase.

References

[1] R.J. Turnbull, Effect of dielectrophoretic force on the Bénard instability, Phys. Fluids 12 (1969) 1809.
[2] H.N. Yoshikawa, O. Crumeyrolle, I. Mutabazi, Dielectrophoretic force-driven thermal convection in annular geometry, Phys. Fluids 25 (2013) 024106.
[3] B. Chandra, D.E. Smylie, A laboratory model of thermal convection under a central force field, Geophys. Fluid Dyn. 3 (1972) 211–224.
[4] V. Travnikov, O. Crumeyrolle, I. Mutabazi, Numerical investigation of the heat transfer in cylindrical annulus with a dielectric fluid under microgravity, Phys. Fluids 27 (2015) 054103.
[5] B. Futterer, C. Egbers, N. Dahley, S. Koch, L. Jehring, First identification of sub- and supercritical convection patterns from 'GeoFlow,' the geophysical flow simulation experiment integrated in Fluid Science Laboratory, Acta Astronaut. 66 (2010) 193.
[6] B. Futterer, A. Krebs, A.C. Plesa, F. Zaussinger, R. Hollerbach, D. Breuer, C. Egbers, Sheet-like and plume-like thermal flow in a spherical convection experiment performed under microgravity, J. Fluid Mech. 735 (2013) 647.
[7] B. Sitte, H.J. Rath, Influence of the dielectrophoretic force on thermal convection, Exp. Fluids 34 (2003) 24.
[8] N. Dahley, B. Futterer, C. Egbers, O. Crumeyrolle, I. Mutabazi, J. Phys. Conf. Ser. 318 (2011) 082003.
[9] L.D. Landau, E.M. Lifshitz, Electrodynamics of Continuous Media, Landau and Lifshitz Course of Theoretical Physics, vol. 8, 2nd ed., Elsevier Butterworth–Heinemann, Burlington, MA, 1984.
[10] A. Bahloul, I. Mutabazi, A. Ambari, Codimension 2 points in the flow inside a cylindrical annulus with a radial temperature gradient, Eur. Phys. J. Appl. Phys. 9 (2000) 253–264.
[11] G. de Vahl Davis, R.W. Thomas, Natural convection between concentric vertical cylinders, Phys. Fluids 12 (Suppl. II) (1969) 198–207.